Macromolecules

Article

Cite This: Macromolecules 2018, 51, 2723−2731

# Low-Temperature Ionic Conductivity Enhanced by Disrupted Ice Formation in Polyampholyte Hydrogels

Xinda Li,[†] Hemant Charaya,[†] Guy M. Bernard,[‡] Janet A. W. Elliott,[†] Vladimir K. Michaelis,[‡] Byeongdu Lee,*[,§] and Hyun-Joong Chung*[,†]

[†]Department of Chemical and Materials Engineering, University of Alberta, Edmonton, Alberta T6G 1H9, Canada

[‡]Department of Chemistry, University of Alberta, Edmonton, Alberta T6G 2G2, Canada

[§]Advanced Photon Source, Argonne National Laboratory, Argonne, Illinois 60439, United States

Supporting Information

**ABSTRACT:** The phase behavior of water in hydrogels has a broad impact on many health and energy applications. Our previous study showed that polyampholyte hydrogel has the potential to be used as an aqueous gel electrolyte in electrochemical storage devices at −30 °C due to enhanced low-temperature conductivity. In this study, we detail the impact polymer structure has on this enhanced conductivity, explaining this finding with a model charge-balanced polyampholyte, poly(4-vinylbenzenesulfonate-*co*-[3-(methacryloylamino)propyl]trimethylammonium chloride), a hydrogel whose polymer and water structures are probed by variable-temperature SAXS, WAXS, and solid-state NMR spectroscopy. SAXS results at room temperature indicate a networked globule structure in the charge-balanced polyampholyte hydrogels. The globular radius of gyration is ∼2.5 nm, whereas the globular size and its clustering structure are dependent on synthesis parameters. Variable-temperature SAXS data reveal a temperature-dependent structure evolution of the polyampholyte hydrogel. An interconnected globular network structure of polymer-rich phase at low temperature, observed by electron microscopy, is suggested to preserve ion-conducting channels of nonfrozen water molecules at low temperatures. This hypothesis is further supported by solid-state NMR spectroscopy. Together these findings provide macromolecular- and molecular-level insight that may be used to design gel electrolytes for enhanced low-temperature performance.

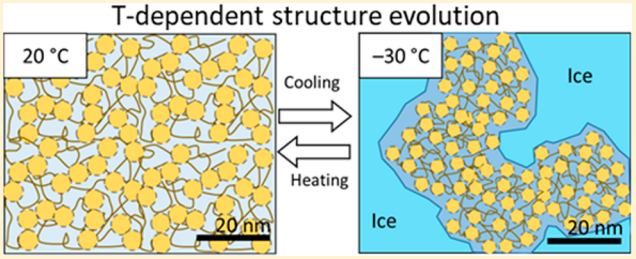


## INTRODUCTION

Tough hydrogels, mechanically soft but robust and tear-resistant materials in which hydrophilic polymer networks hold more water than the original polymer weight, are a promising class of materials for bioimplantable electronics, sensors/actuators in soft machines, surgical glues, and gel electrolytes for energy storage devices.[1−3] As these materials are inherently rich in water content, understanding the phase behavior of water in the polymer network has important implications for low-temperature applications where freezing of water can be detrimental. It is known that nanoscale confinement[4−6] and controlled hydrophilicity/phobicity[7] are effective strategies to control freezing behavior. Recently, Vogt and collaborators studied the dynamics of supercooled water molecules under nanoscale confinement within the cluster of hydrophobic domains and its impact on the antifreezing behavior within hydrogels.[8]

Polyampholytes, a subclass of polyelectrolytes, are macromolecules that contain both acidic and basic groups that may produce positive and negative electrostatic charges, respectively, as a response to the surrounding environment.[9,10] The high density of the distributed opposite charges in polyampholyte chains introduces ionic cross-linking that can lead to well-defined three-dimensional structures in foldamers,[11] DNA condensation, and protein folding.[12] Recently, synthetic polyampholytes have shown various potential applications such as mechanically tough and self-healable hydrogels,[13−15] antibiofouling coating,[16] thermosensitive smart optical coating,[17] and self-adjustable adhesives.[18]

We have previously shown that polyampholyte hydrogel also has the potential to be used as an aqueous gel electrolyte in electrochemical storage devices.[19] In that work, a supercapacitor that employed a polyampholyte hydrogel electrolyte filled with 16.8 wt % potassium hydroxide rendered an enhanced specific capacitance of 75 F/g at −30 °C, whereas a control sample with the aqueous electrolyte without the polymer showed 24 F/g under identical conditions. As another example in this work, temperature-dependent ionic conductivities of a 10 wt % NaCl solution, a hydrogel precursor solution with 10 wt % NaCl (SOL-10-2.1; sample nomenclature in Table S1 of the Supporting Information), and polyampholyte hydrogel with 10 wt % NaCl (PA-10-2.1) are shown in Figure 1. With decreasing temperature, the ionic conductivity of the NaCl solution decreased gradually

Received: November 26, 2017
Revised: February 24, 2018
Published: March 30, 2018





DOI: 10.1021/acs.macromol.7b02498
Macromolecules 2018, 51, 2723−2731

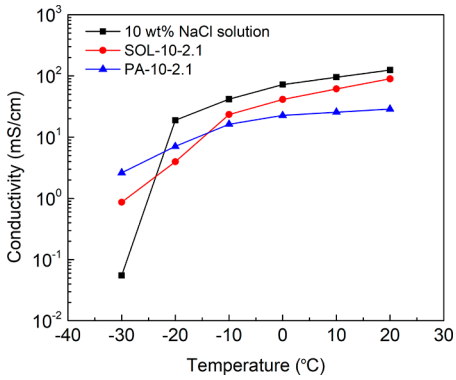


**Figure 1.** Ionic conductivities of an aqueous 10 wt % NaCl solution, the NaCl solution mixed with monomeric precursor molecules (SOL-10-2.1), and the NaCl solution in polymerized hydrogel (PA-10-2.1) plotted against temperature.

from 124.58 to 18.85 mS/cm (15% of +20 °C value) between +20 and −20 °C, respectively, and then dropped drastically to 0.055 mS/cm (0.045%) at −30 °C. The eutectic temperature (−21 °C) in the water−NaCl phase equilibrium, where all remaining liquid transforms to solid, may explain the drastic ionic conductivity drop between −20 and −30 °C. On the other hand, PA-10-2.1 exhibited a gradual decrease in ionic conductivity from 28.78 to 7.07 (24.57%) and then to 2.62 mS/cm (9.10%) at +20, −20, and −30 °C, respectively. The low-temperature conductivity enhancement is much more prominent than that of another control sample, SOL-10-2.1, where the nonpolymerized precursor solution exhibited a limited effect with conductivity values of 89.62, 3.97 (4.43%), and 0.87 (0.97%) for +20, −20, and −30 °C, respectively.

The results shown in Figure 1 suggest two possible reasons for the enhanced ionic conductivity in polyampholyte hydrogels. First, monomeric units in the polyampholyte play a role as additional salts, causing a depression of the eutectic temperature. If osmotic virial coefficients or Margules parameters are available for the monomers, such effects can be quantified by our thermodynamic model.[6,20] However, the solution thermodynamics argument cannot explain the further enhancement of the low-temperature ionic conductivity in the hydrogels. This effect can only be understood when the nanoscopic structure of polymer chains and the status of water molecules are elucidated as a function of temperature.

Experimental studies on the details of hierarchical structures of polyampholytes have, in general, been relatively rare. Nisato et al. proposed a qualitative description of the globular structure of chains in polyampholyte hydrogels based on light scattering and swelling experiments.[21] However, the details of the globular structures, including size and chain density of each globule and the superstructure that the globules may produce, have not been explored. Within the polyampholyte family, the hierarchical structure of polyzwitterions, where both acidic and basic components reside in each repeating monomer unit, has been studied in detail. Polyzwitterions show a unique property called antipolyelectrolyte behavior when the polyampholyte is in an isoelectric state (i.e., the positive and negative charge densities are nearly equal).[22] Whereas ordinary polyelectrolytes undergo a collapse in their chain conformation when the salt concentration increases in the aqueous solution, polyzwitterions exhibit swelling behavior that leads to an increase of the solution viscosity and the solubility of the macromolecular component.[23−26] Moreover, the high polymer concentration in the polyzwitterion hydrogel leads to electrostatically induced hierarchical self-assembly that defines a multiscale structural network in the hydrogel.[22] Safinya and co-workers recently investigated the effect of salt on the hierarchical structural formation of neurofilament hydrogel, whose structural assembly is dictated by ionic interactions between polyampholyte side arm chains. The neurofilament hydrogel (∼5 wt % neurofilament in salt water) undergoes transitions from liquid-crystalline hydrogel to isotropic gel and to nematic hydrogel when the background salt concentration increases.[27]

In this work, we studied the structure of a polyampholyte random copolymer that consists of two oppositely charged ionic monomers, sodium 4-vinylbenzenesulfonate (NaSS) and [3-(methacryloylamino)propyl]trimethylammonium chloride (MPTC), which is denoted as poly(NaSS-*co*-MPTC). Furthermore, we discuss the interactions with water molecules when the charge-balanced polyampholyte formed a hydrogel. Using small- and wide-angle X-ray scattering (SAXS and WAXS) as tools to study polymer network structures and their effects on the phase behavior of water in the hydrogels, we found that a networked globular structure effectively prevented the freezing of water in the hydrogel. There is clear evidence of amorphous water molecules and slushlike, submicrometer-sized ice formation at low temperatures. Solid-state nuclear magnetic resonance (NMR) assisted in identifying dynamic and frozen water within the hydrogels. Analysis of the line shape of the $^2$H NMR spectra (samples prepared in $D_2O$) was particularly useful in assessing the behavior of water in these samples.[28] All these findings are consistent with our observation of the increased ionic conductivity of the hydrogel at low temperatures. It is notable that multiple freeze−thaw cycles did not impact the phase behavior of water in the hydrogel soft materials.

## EXPERIMENTAL SECTION

**Polyampholyte Hydrogel Synthesis.** The protocol as described by Gong et al.[13] was followed to copolymerize sodium 4-vinylbenzenesulfonate (cationic monomer; NaSS) and [3-(methacryloylamino)-propyl]trimethylammonium chloride (anionic monomer; MPTC) with Irgacure 2959 (photoinitiator) and NaCl. The chemicals were purchased from Sigma-Aldrich and used as received. The aqueous precursor solution with designed chemical concentrations (shown in Table S1) was injected into the gap between two glass plates separated by a 1 mm thick Teflon spacer. The monomer polymerization was initiated by irradiating the sample with UV light with a lamp-to-sample distance of 5 mm (UV broadband lamp with a maximum peak at 365 nm with an intensity of 22 mW cm$^{-2}$; Jelight UVO-Cleaner Model-342, USA).

**Variable-Temperature Small- and Wide-Angle X-ray Scattering Characterization.** SAXS/WAXS samples were made by irradiating beeswax-sealed glass capillaries (Charles Supper, USA) containing a precursor solution with UV. The SAXS experiments were performed with the beamline 12-ID-B of the Advanced Photon Source at the Argonne National Laboratory in the USA. The 14 keV X-ray beam was exposed to the 1.5 mm diameter capillary sample with an exposure time of typically 0.1 s. Scattered X-ray photons were measured with a Pilatus 2M (Dectris Ltd.) detector located about 2 m downstream of the sample. Ten images per sample were collected and averaged to confirm that no beam damage had occurred and to increase counting statistics. Background scattering from a capillary containing water was subtracted from sample data. In the temperature-dependent SAXS/WAXS measurements, the following thermal history was programmed: (i) held at 5 °C for 10 min, (ii) cooled from +5 to −40 °C at a rate of 5 °C/min, (iii) held at −40 °C for 10 min, and (iv) heated to 5 °C at a rate of 1 °C/min. The empty capillary was used as a background. In addition to that, the water scattering measured at 0 °C was subtracted. We note that the scattering of water in SAXS is mainly from its density fluctuation and


DOI: 10.1021/acs.macromol.7b02498
Macromolecules 2018, 51, 2723−2731

thus proportional to the amount of liquid water. Since the amorphous water content varies with temperature, we scaled the water scattering by the relative amount of amorphous water determined from the WAXS amorphous halo to the value at 0 °C.

**Development of SAXS Theory for Clusters: Model.** The intensity from a model cluster containing $N$ spheres that are primary particles ($N$ = 10 for the model in Figure S4) can be numerically calculated with the general theory

$$I(q) = \int \sum_{k=1}^{N} F(q, R_k) e^{-j\mathbf{q}\cdot\mathbf{r}_k} \, d\Omega \tag{1}$$

where $R_k$ and $\mathbf{r}_k$ are the radius and position of the $k^{th}$ sphere. The 1D scattering vector $q$ is the magnitude of the 3D scattering vector $\mathbf{q}$. The integration over dΩ stands for orientational average. The form factor can be calculated as

$$P(q) = \sum_{k=1}^{N} |F(q, R_k)|^2 \tag{2}$$

where $F(q,R)$ is the spherical Bessel function for a sphere with radius $R$.

Finally, simulated $I(q)$ and $P(q)$ are shown in Figure S5a. The calculated $I(q)$ shows clearly three regions separated by the positions denoted by closed and open arrows. The smallest $q$ region is the Gunier region for the cluster, which is in this case the 1D array. The highest $q$ region is the region where the primary particle scattering dominates. The Porod region of the cluster that exhibits power-law slope of −1 locates between the two regions.

**Structure Factor Derivation in Our Model.** The structure factor of the primary spheres forming the 1D array can be obtained by $I(q)/P(q)$, which is shown in Figure S5b. Analytically, the structure factor $S(q)$ can be calculated by orientational averaging:[29−31]

$$S(\mathbf{q}) = 1 + \int f(\mathbf{r}) n_\infty(\mathbf{r}) e^{-j\mathbf{qr}} \, d\mathbf{r} \tag{3}$$

where $f(\mathbf{r})$ is the shape function of the cluster and $n_\infty(\mathbf{r})$ is the pair correlation function of the primary particles assuming that they fill infinite space with keeping the same positional statistics or nature. The second terms can be written using the convolution theorem of Fourier transforms:[32]

$$\int f(\mathbf{r}) n_\infty(\mathbf{r}) e^{-j\mathbf{qr}} \, d\mathbf{r} = \int f(\mathbf{r}) e^{-j\mathbf{qr}} d\mathbf{r} \otimes \int n_\infty(\mathbf{r}) e^{-j\mathbf{qr}} \, d\mathbf{r} \tag{4}$$

where the operator ⊗ stands for convolution. The first term on the right, Fourier transform of $f(\mathbf{r})$, is the form factor of the cluster which we define as

$$\int f(\mathbf{r}) e^{-j\mathbf{qr}} \, d\mathbf{r} \equiv P_c(\mathbf{q}) \tag{5}$$

The second term on the right, Fourier transform of $n_\infty(\mathbf{r})$, can be further broken down into two components, interference function and null scattering terms, by employing the mean particle number density $n_c$:

$$\int n_\infty(\mathbf{r}) e^{-j\mathbf{qr}} \, d\mathbf{r} = \int (n_\infty(\mathbf{r}) - n_c) e^{-j\mathbf{qr}} \, d\mathbf{r} + N\delta(\mathbf{q}) \tag{6}$$

We define the interference function as

$$\int (n_\infty(\mathbf{r}) - n_c) e^{-j\mathbf{qr}} \, d\mathbf{r} \equiv i_i(\mathbf{q}) \tag{7}$$

Since

$$P_c(\mathbf{q}) \otimes (N\delta(\mathbf{q})) = NP_c(\mathbf{q}) \tag{8}$$

the structure factor is finally written as below:[29,33]

$$S(\mathbf{q}) = 1 + P_c(\mathbf{q}) \otimes i_i(\mathbf{q}) + NP_c(\mathbf{q}) \tag{9}$$

The interference function is expressed as $i_i(\mathbf{q}) = S_i(\mathbf{q}) - 1$, and $S_i(\mathbf{q})$ is the structure factor of the infinite number of primary particles. So we consider $S_i(\mathbf{q})$ as the structure factor for internal arrangement of the primary particles in the cluster.

The role of the convolution in the second term is to broaden the peaks and valleys of the interference function. Considering that the structure factor of primary particles forming nonregular cluster is already broad, we might simply neglect it. For high $q$ region, where $i_i(\mathbf{q}) > NP_c(\mathbf{q})$, $1 + P_c(\mathbf{q}) \otimes i_i(\mathbf{q})$ can be approximated as $S_i(\mathbf{q})$. For thesmall $q$ region, where $i_i(\mathbf{q}) < NP_c(\mathbf{q})$, $1 + NP_c(\mathbf{q})$ can be approximated as $fP_c(\mathbf{q})$, where $f = N - 1$. Since the orientational average can be performed independently for each term, we can approximate $S(q)$ as

$$S'(q) = \begin{cases} fP_c(q) & q < q_c \\ S_i(q) & q > q_c \end{cases} \tag{10}$$

where $q_c$ is a crossover $q$ that separates the high and small $q$ regions. In this work, we smoothed the transition at $q_c$ by adding a smoothing function, for example

$$S(q) = S'(q) + \left(|fP_c(q) - S_i(q)| + \frac{3}{2}\right)^{-4} - \left(\frac{5}{2}\right)^{-4} \tag{11}$$

When $fP_c(q)$ is not significant compared to $S_i(q)$ in the high $q$ region, we may simplify $S(q)$ to

$$S(q) = fP_c(q) + S_i(q) \tag{12}$$

**Comparison with Simulation.** In order to simulate $S(q)$ for our 1D array cluster, we employed the Guinier−Porod equation for $P_c(q)$ (blue dotted curve at the bottom of Figure S5). The Guinier−Porod equation for a finite sized object requires two parameters: the radius of gyration $R_{g,c}$ and the Porod exponent $P$. In this work, the radius of gyration of the 1D array is calculated as $L/\sqrt{12}$. The Porod exponent is 1 since it is a 1D structure. $f$ is about 9 because of 10 particles (a bit larger than 9 due to polydispersity). The second term, $S_i(q)$, is to describe the structure factor of particles within the array. We employed the structure factor equation of the Percus−Yevick hard sphere potential (magenta dotted curve at the bottom of Figure S5). We define $q_c$ for $q$ where $fP_c(q) = S_i(q)$.

**Ionic Conductivity Measurement.** Ionic conductivity measurements of the NaCl and precursor solutions, as well as the polyampholyte hydrogel, were undertaken using screen-printed electrodes (DRP-150, DROPSENS, Spain) in a three-electrode configuration by electrochemical impedance spectroscopy (EIS, PGSTAT302N, Metrohm Autolab, Netherlands). The frequency range for EIS measurements was from 100 kHz to 10 mHz, where an open circuit potential mode with an ac perturbation of 5 mV was used. The temperature was regulated using a temperature-controlled chamber (TS102G, Instec Inc., USA). The sample temperature was decreased from 20 to −30 °C at a rate of 5 °C/min and held at −30 °C for 10 min, followed by the EIS measurement. After each measurement, the sample was heated at a rate of 1 °C/min to the next desired temperature. The hydrogel samples were placed on top of the screen-printed electrode and compressed to ensure an intimate contact between the electrode and the hydrogel. For solution measurements, a reservoir (depth 1 mm, area 10 × 10 mm$^2$) made by a spacer was used to contain the electrolyte solution. EIS results were fit with the Randles circuit model using software (Autolab NOVA) to determine the electrolyte resistance, which was converted into ionic conductivity based on the cell constant of the measurement setup.

**Field Emission Scanning Electron Microscope (FE-SEM) Characterization.** For the FE-SEM sample preparation, two PA-10-2.1 samples were cooled from room temperature to 20 and −30 °C, at a rate of 1 °C/min using a temperature-controlled chamber, and held at the desired temperature for 30 min. After that, the samples were taken from the chamber and immediately quenched in liquid nitrogen, followed by freeze-drying in a freeze-dryer (Super Modulyo, Savant). An ∼5 nm thick Au layer was coated on the freeze-dried samples using a gold sputter unit (Denton; USA). An FE-SEM (Zeiss, Sigma) was utilized for the morphological study.

**Solid-State NMR.** $^1$H and $^2$H NMR measurements were conducted at 11.75 T on a Bruker Avance spectrometer, operating at 500.3 and 76.8 MHz, respectively. Samples were packed in 4 mm zirconia rotors, and spectra were obtained with a Bruker 4 mm MAS probe operating in double resonance mode. $^1$H NMR spectra were obtained with a Bloch



DOI: 10.1021/acs.macromol.7b02498
Macromolecules 2018, 51, 2723−2731

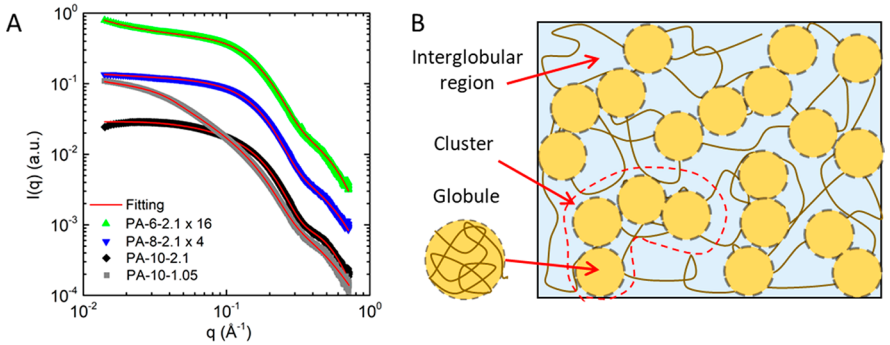


**Figure 2.** (A) SAXS data for PA-6-2.1, PA-8-2.1, PA-10-2.1, and PA-10-1.05. The red lines are the fits of the experimental data. (B) Schematic illustration of the polyampholyte hydrogel. The hydrogel consists of globules (i.e., nanoscale hydrated particle-like structures with high polymer concentration) separated by water-rich domains (i.e., interglobular regions with low polymer concentration). The polymer globules aggregate to form clusters. See text for details.

**Table 1. Fitting Parameters for SAXS Results**

| | cluster | | | | | | primary particle (globule) | | | |
|---|---|---|---|---|---|---|---|---|---|---|
| sample | $f$ | $R_{g,c}$ (Å) | $P$ | $R_h$ (Å) | $\nu$ (%) | $f_p$ (au) | $\bar{R}_p$ (Å) | $\sigma_p$ (Å) | $D_f$ | $R_{g,p}$ (Å) |
| PA-6-2.1 | ≪1 | ≫10 | 1.3 | 22.6 | 1.9 | 0.034 | 18.1 | 5.8 | 1.9 | 23.4 |
| PA-8-2.1 | ≪1 | ≫10 | 1.3 | 15.0 | 1.8 | 0.035 | 18.2 | 6.0 | 1.5 | 24.0 |
| PA-10-2.1 | 1.2 | 13.1 | 1.2 | | 0 | 0.024 | 18.1 | 4.7 | 1.8 | 20.2 |
| PA-10-1.05 | 9.0 | 31.1 | 1.0 | | 0 | 0.012 | 17.8 | 5.2 | 1.8 | 21.4 |

pulse, using a 4.0 $\mu$s 90° pulse, a 2.0 s acquisition time, and a 1.0 s recycle delay. Room temperature $^2$H NMR spectra were also obtained using a Bloch pulse, using a 2.5 $\mu$s pulse corresponding to a 45° flip angle, with an acquisition time of 2.0 s and a 1.0 s recycle delay. Nonambient temperature $^2$H NMR spectra were obtained with a solid-echo pulse sequence: 90°−$\tau_1$−90°−$\tau_2$−AQ, where $\tau_1$ is the interpulse delay and $\tau_2$, the refocusing delay, was set to a low value, and data were left-shifted to ensure the FID began at its maximum. The 90° pulses were 5.0 $\mu$s, $\tau_1$ was 20.0 $\mu$s, the acquisition time was 16 ms, and the recycle delay was 1.0 s. Variable-temperature NMR data were obtained on the Avance 500 NMR spectrometer using the BVT 3000 VT unit provided by Bruker Biopsin. An ethanol/dry ice bath was used as the heat exchanger source, with dry air as the VT gas, whose flow rate was 1600 L/h. The temperature was calibrated based on the temperature dependence of the $^{207}$Pb chemical shifts of methylammonium lead chloride, following a protocol recently developed in the coauthors' laboratory.[34]

## RESULTS AND DISCUSSION

A one-step random copolymerization method previously developed by Gong et al.[13] was adopted for our synthesis of the poly(NaSS-*co*-MPTC) hydrogel to produce a charge-balanced system with a random monomer sequence. Briefly, NaSS, MPTC, NaCl, and a photoinitiator were dissolved in deionized water (DIW). The precursor solution was injected into a gap, created with a 1 mm spacer, between two glass plates. UV irradiation transformed the precursor solution into a polyampholyte hydrogel. In all cases, the ratios of monomers between NaSS and MPTC were held at the experimentally determined charge-balanced point, as shown in the Supporting Information. Both solution $^1$H NMR spectroscopy and hydrogel leaching tests confirmed that the monomer conversion of NaSS and MPTC was ∼98% (Supporting Information). Swelling experiments also confirmed that these polyampholytes are strictly charge balanced. Hereafter, we denote the samples using the code PA-#-*c*, where the # is the NaCl concentration (wt %) in the polyampholyte hydrogel and *c* is the total monomer concentration (M).

SAXS analyses were used to determine the structure of the as-prepared polyampholyte with different NaCl concentrations. The SAXS results shown in Figure 2A, measured on the as-prepared samples, reveal that the samples all contain molecular aggregates forming spherical objects consisting of Gaussian chains, as evidenced by the high $q$ power-law slope of −2 (see fractal power-law exponent $D_f \sim 2$ in Table 1).[35] In other words, the primary particles are in a well-solvated state (i.e., polymer-rich water-containing domains). The shape of the primary particles is believed to be spherical since no power-law scattering was found in the very small $q$ region; therefore, we denote the primary particle as a globule. For some samples, the spherical form factor scattering alone did not fit the intensity profile in the small $q$ regions, $q < 0.2$ Å$^{-1}$, indicating that the globular primary particles form a nanoscale cluster.

To analyze the hierarchical structure, we developed the following SAXS model (see the details in the experimental section):

$$I(q) = (\Delta\rho)^2 f_p P(q; \bar{R}_p, \sigma_p, D_f) S(q) \quad (13)$$

where $(\Delta p)^2$ and $f_p$ are the X-ray scattering contrast and the number concentration (e.g., molar concentration) of primary particles, respectively. When $I(q)$ for a sample is measured on an absolute scale, one can determine $f_p$ if $(\Delta p)^2$ is known for the sample. In our experiment, $I(q)$ is measured in arbitrary units. Since we normalized $I(q)$ by the sample thickness, the *relative* values of $f_p$ are meaningful, assuming that $(\Delta p)^2$ does not vary from sample to sample. The form factor of a primary particle $P(q)$ is modeled as that for polydisperse spheres with fractal internal structure.[28] The fractal power-law exponent $D_f \sim 2$ (*vide supra*) indicates that the internal structure of the primary particle is Gaussian-chain-like.[36] The size distribution of the primary particles is modeled by the two parameters of the Schultz−Zimm size distribution; $\bar{R}_p$ and $\sigma_p$ are the mean radius and variance of the external size of the primary particles, respectively. $R_{g,p}$ is the radius of gyration of the primary particle calculated from $\bar{R}_p$ and



DOI: 10.1021/acs.macromol.7b02498
*Macromolecules* 2018, 51, 2723−2731

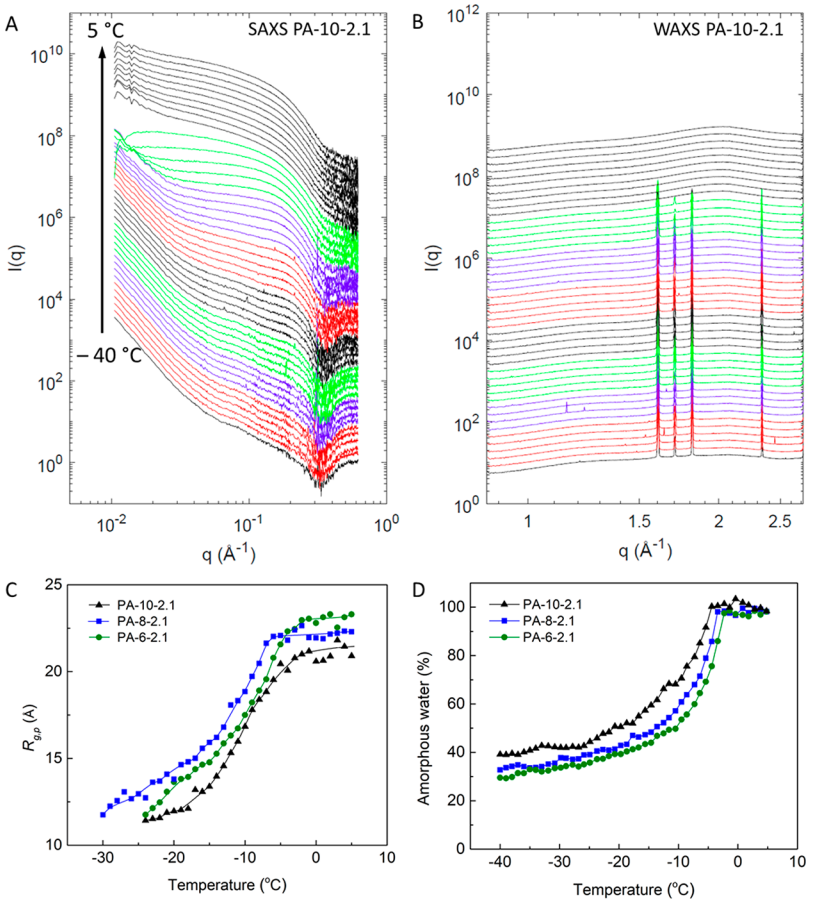


**Figure 3.** (A, B) Variable-temperature SAXS and WAXS results of PA-10-2.1, respectively. These spectra were collected at various temperatures from −40 to 5 °C with an interval of 1 °C at a ramping rate of 1 °C/min. (C) $R_{g,p}$ of globules and (D) normalized amounts of amorphous water in the polyampholyte hydrogel versus temperature. Solid lines are provided as guides to the eye.

$\sigma_p$. Since the primary particles are aggregated to form clusters, the structure factor $S(q)$ is defined to include the hierarchical structure as

$$S(q) = fP_c(q; R_{g,c}, P) + S_i(q; R_h, \nu) \quad (14)$$

where $P_c$ is the form factor of a cluster, which is calculated using the Guinier−Porod model.[36,37] It has two variables $R_{g,c}$ and $P$, which are radius of gyration and the Porod constant of the cluster, respectively. At $q = 0$, $P_c = 1$, and $f$ is a scaling factor of the cluster form factor. In this definition, $f + 1$ denotes the mean number of primary particles forming a cluster.[36] The Percus−Yevick (PY) hard sphere structure factor $S_i(q;R_h,\nu)$ is added to describe the internal arrangement of the primary particles in a cluster.[36] $R_h$ and $\nu$ are the hydrodynamic radius and volume fraction of the primary particles in a cluster, respectively (Figure S6).

Although the very low $q$ scattering ($q$ < 0.02 Å$^{-1}$) is not modeled due to the experimental resolution limit, it may provide a clue on structures larger than hundreds of nanometers. For instance, the low $q$ upturn of the SAXS data for the PA-6-2.1 samples indicates macroscopic separation between water- and globule-rich domains. This can be understood considering that in polyampholytes synthesized by random polymerization of positively and negatively charged groups the net charge of each globule varies and is typically not zero.[10] At low salt concentration, the reduction of salt screening effects leads to a tendency for globules to form an aggregated superstructure, as observed in dilute polyampholyte solution.[38]

The effect of polymer concentration on the polyampholyte hydrogel structure was also studied by varying the monomer concentration in the precursor solutions. The fitting of SAXS profiles for PA-10-1.05 and PA-10-2.1 in Figure 2A indicates that both hydrogels form globules with an ∼5 nm diameter primary unit. A slightly larger $D_f$ for PA-10-1.05 than for PA-10-2.1 indicates that the monomer density in the globules is much lower for the former. Interestingly, those globules in PA-10-1.05 are aggregated into a 1D array as noticed from the Porod constant $P$ ∼ 1 for the cluster (Table 1), and the array consists of about 10 globules as seen from parameter $f$ in Table 1. Assuming the shape of the cluster is a cylinder with its cross section identical to the cross section of the globules, its length can be calculated to be ∼10 nm based on its radius of gyration using the relation $R^2_{g,\text{cylinder}} = \frac{R^2}{2} + \frac{L^2}{12}$, where $R$ is the cylinder radius and $L$ is the length of a cylindrical rod. Since 10 nm is rather short for 10 globules in a row, the 1D array of globules is not likely rigid-rod-like but a more flexible necklace.

On the basis of these findings, we can draw a schematic cartoon model of the polyampholyte chain networks, as seen in Figure 2B. Here, the charge-balanced polyampholyte chains form a networked structure of globules; the globules are spherical in shape, hydrated, on the nanoscale, contain polymer-rich domains, and are interconnected to each other by polymer chains. The interglobular regions are denoted as water-rich



DOI: 10.1021/acs.macromol.7b02498
Macromolecules 2018, 51, 2723−2731

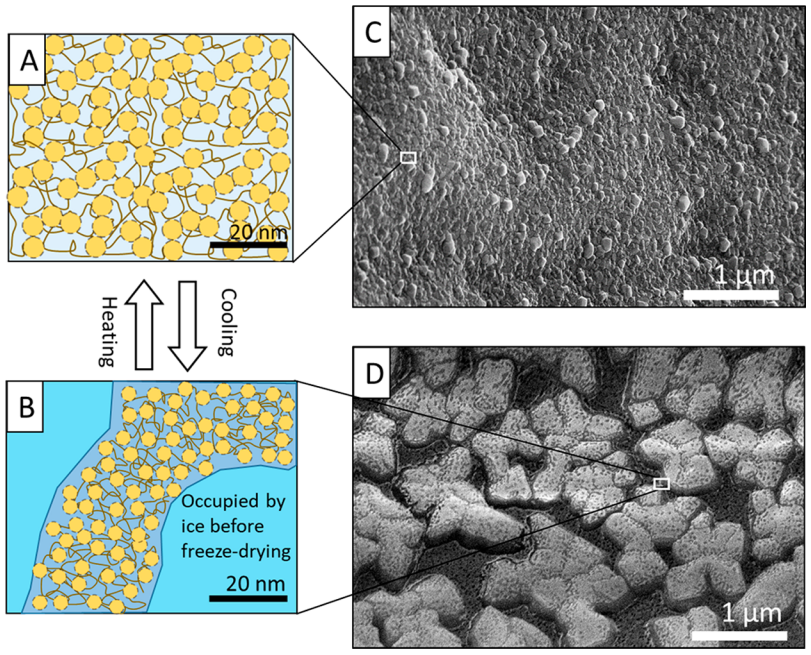


**Figure 4.** Temperature-dependent structural evolution of salt-containing polyampholyte hydrogel at (A) 20 °C and (B) − 30 °C. Yellow circles in hatched outlines denote polymer-rich, but hydrated, globules. Cross-sectional FE-SEM images of PA-10-2.1 (C) at 20 °C and (D) prefrozen at −30 °C, followed by quenching in liquid nitrogen and freeze-drying. (A) and (B) represent the hydrogel structures of regions identified by the white boxes in (C) and (D), respectively.

domains. The globule is similar to the case of a charge-balanced polyampholyte chain structure in the dilute solution.[10] It has been theoretically predicted that a charge-balanced polyampholyte chain forms a globular conformation because Debye−Huckel fluctuation induces attraction between charges. The size of the globule depends on ionic strength and on the number of repeating units of the polymer.[10,39] In our hydrogels, the concentrations of polyampholytes are much higher than concentrations of dilute solutions. Thus, a globule consists of several chains, while each chain may belong to a few neighboring globules simultaneously, resulting in a networked superstructure of globules. This feature is similar to the qualitative description suggested by Nisato et al.[21] as well as to the ionic clusters in ionomers (e.g., Nafion) due to the self-assembly of charged polymer chains.[40,41] Both $R_{g,p}$ and the number of globules decrease with increasing NaCl concentration, as shown in Table 1. This implies that electrostatic interactions between oppositely charged chains become weaker because higher ionic strength would screen charges on the chains more efficiently. In other words, with increased salt ions, more polyampholyte chains tend to exist in the water-rich domain rather than to form globules.

The structures of polymer and water molecules at low temperatures were surveyed simultaneously using SAXS and WAXS, respectively; these spectra were collected at various temperatures from −40 to 5 °C with an interval of 1 °C at a ramping rate of +1 °C/min. In our work, we focused on melting behavior upon slow heating, as we attempted to extract the information under (nearly) equilibrium conditions; our study does not focus on ice crystallization or nucleation kinetics of confined water that occur in cooling processes. Figures 3A and 3B show examples of SAXS and WAXS spectra of PA-10-2.1, respectively. Figure 3C shows the $R_{g,p}$ of globules in the polyampholyte hydrogel. The radius of gyration increased with increasing temperature, with the resolution limit of the smallest discernible $R_{g,p}$ being ∼10 Å. From the WAXS results, the relative amount of amorphous water was extracted by integrating the areas of the diffraction peaks for amorphous water (the hump located between 1.5 and 2.5 $Å^{-1}$), as shown in Figure 3D. These values were normalized by sample thickness, polymer concentration, and minor beam intensity fluctuation. WAXS results indicate that a higher fraction of water molecules appear to be amorphous at a given low temperature when the hydrogel contains a higher NaCl concentration.

On the basis of the variable temperature SAXS/WAXS results, we propose a qualitative description of the structural evolution of polymers and the behavior of water molecules in ice-forming polyampholyte hydrogels in Figures 4A and 4B. Upon cooling, the water molecules in interglobular regions (i.e., water-rich domains) start to form ice. Water molecules trapped within the globules do not form ice because they cannot align themselves to form a periodic crystalline environment, due either to a strong confinement between the polymer chains or to a strong interaction with these chains. As ice crystals grow, the hydrated globules (i.e., polymer-rich domains), which do not participate in the ice formation, come closer to each other. At the same time, the concentration of NaCl in the non-ice region becomes elevated, which increases electrostatic screening effects between the globules, leading to a better dispersion of the globules and to a further reduction in globular size. Finally, ice crystals are inhibited from growing freely in size because of steric hindrance from the nonfreezable globules and the polyampholyte networks between them that distribute across the entire hydrogel.

Direct visualization by microscopic techniques can be an effective method for confirming the morphological hypothesis based on spectroscopic methods. The SEM images in Figures 4C and 4D were obtained by liquid nitrogen quenching followed by freeze-drying to visualize mesoscopic polymer structures after sublimating water molecules. Here, the sample in Figure 4C was quenched from room temperature; a homogeneous distribution of fine nanostructures is found in the freeze-dried hydrogel. On



DOI: 10.1021/acs.macromol.7b02498
*Macromolecules* 2018, 51, 2723−2731

the other hand, in Figure 4D, a SEM image of a sample that was prefrozen at −30 °C before quenching with liquid nitrogen, stark differences in morphology are observed. Here, the darker trenches are attributed to sublimated, submicrometer-sized, slushlike ice domains between polymer-rich domains. The brighter regions correspond to the polymer-rich ice-free domain regions that are interconnected. Finally, it is notable that this temperature-dependent structure evolution of a salt-containing polyampholyte hydrogel is reversible (as evidence, see the DSC scanning of multiple freezing−thawing cycles shown in Figure S3).

To investigate the hypothesis that the interconnected polymer-rich domains play a role as channels for ionic conduction at low temperatures, nonspinning $^{1}$H solid-state NMR spectra of PA-10-2.1 and of its precursor solution were acquired 21 °C (Figure 5). These contain relatively well resolved

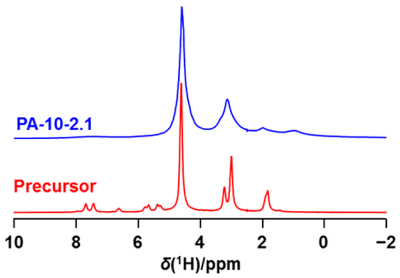


**Figure 5.** Nonspinning $^{1}$H solid-state NMR spectra of PA-10-2.1 (upper trace) and of the corresponding precursor solution (lower trace) acquired at 21 °C at 11.75 T.

peaks, although in the case of PA-10-2.1, some broadening of all peaks is observed. The peak at 4.6 ppm is attributed to $H_2O$. In their investigation of poly(*N*-isopropylacrylamide) gel networks, Wang et al.[42] found that peaks attributed to free and bound water were separated by 0.09 ppm, as resolved by high-resolution measurements at 600 MHz. Unfortunately our $^{1}$H resolution was insufficient to determine whether both types of water exist at room temperature. To investigate the status of water in these samples at lower temperatures, $^{2}$H solid-state NMR spectra of PA-10-2.1 (prepared with $D_2O$) were obtained in the 20 to −54 °C temperature range (Figure 6). Spectra obtained at 20 and −5 °C consist of a relatively sharp peak with a $^{2}$H chemical shift near that expected for $D_2O$. At −19 °C, this peak is somewhat broadened, but more importantly, the onset of a broad underlying powder pattern is detected (see the inset to Figure 6B). At −54 °C, the intensity of this pattern begins to dominate and, with a breadth between its extremities exceeding 150 kHz, is comparable to those reported for hexagonal $D_2O$ between −10 and −196 °C.[43,44] Nevertheless, though broadened, the central peak, with line widths at half-maximum of 4.5 kHz, suggests that water mobility persists at −54 °C. A similar pattern was observed for the precursor, as illustrated in Figure S11.

The solid-state NMR observations are consistent with the SAXS/WAXS data discussed above. The $^{1}$H solid-state NMR spectra obtained at room temperature suggest mobile water, with broadened peaks for the PA-10-2.1 sample a possible indication of a slight restriction in the motion. At lower temperature, the $^{2}$H spectra indicate frozen water, consistent with the water-rich domains suggested from the SAXS/WAXS data. The hypothesis that a certain fraction of water molecules do not freeze due to confinement with the polymer chains or interactions with these chains is also verified by this data. The presence of two distinct feature types in the $^{2}$H spectra rather than a continuum from a broad pattern to sharp peaks suggests two distinctive statuses for the water molecules.

Finally, the enhanced ionic conductivity in polyampholyte hydrogels at −30 °C in Figure 1 can be explained by our comprehensive experimental results from SAXS, WAXS, FE-

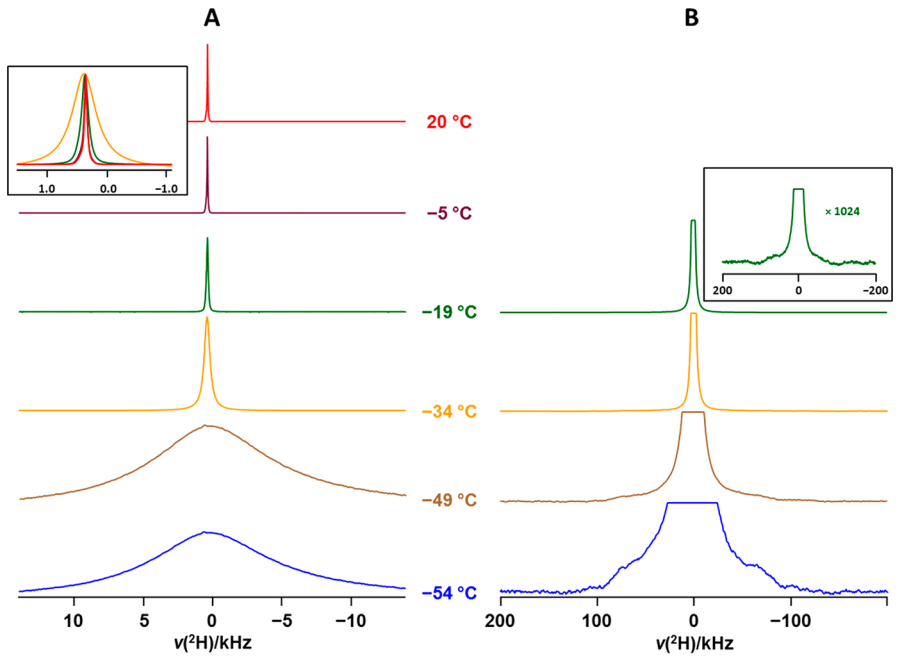


**Figure 6.** Variable-temperature $^{2}$H NMR spectra of nonspinning PA-10-2.1 acquired at 11.75 T at the indicated temperatures. (A) The central peak attributed to mobile water (see text); the inset on the left is an overlay of spectra acquired in the 20 to −34 °C range. (B) Spectra have been multiplied by a factor of 16 (1024 for the spectrum shown in the inset) to illustrate the broad underling powder pattern found for spectra acquired at lower temperatures.



DOI: 10.1021/acs.macromol.7b02498
*Macromolecules* 2018, 51, 2723−2731

SEM, and solid-state NMR. SAXS results suggest that polyampholyte hydrogels in high salt concentration exhibit unique internal structure that even polymer-rich regions consist of highly hydrated globular structure. At low temperatures, the polymer-rich regions keep submicrometer-sized domain structure, which hinders the growth of ice crystals that are fragmented as slush-like structures, as shown by FE-SEM. Moreover, the existence of amorphous water molecules and the mobility of these molecules at temperatures as low as −49 °C are confirmed by WAXS and solid-state NMR. An ion's mobility ($u$) and its molar conductivity ($\lambda$) have the relationship $\lambda = zuF$, where $z$ is the charge number and $F$ is Faraday's constant.[45] Because of the existence of mobile water in interconnected polymer-rich domains at low temperatures, the mobility of $Na^+$ and $Cl^-$ ions in PA-10-2.1 is elevated compared to the frozen control sample of 10 wt % NaCl solution in Figure 1, leading to a 48× increase in the ionic conductivity value.

## CONCLUSIONS

The SAXS results suggest a network of globule structures in the charge-balanced polyampholyte hydrogels with the hydrogel structure being dependent on the synthesis procedure. The globular network structure results in increase in amorphous water −30 °C, as supported by WAXS results. Based on variable-temperature SAXS, WAXS, SEM, and solid-state NMR data, morphological evolution of polyampholyte hydrogel and the behavior of water molecules upon cooling−heating cycles are studied. It is proposed that the interconnected polymer-rich domains result in a slush-like ice formation that allows enhanced ionic conductivity of the hydrogel in ice forming conditions at low temperatures. This observation sheds light on the development of high conductivity gel electrolytes for operations in low temperatures as well as the development of antifreezing surface coatings.

## ASSOCIATED CONTENT

### Supporting Information

The Supporting Information is available free of charge on the ACS Publications website at DOI: 10.1021/acs.macromol.7b02498.

Sample details; NaCl concentration calculation in the as-prepared hydrogel; the total monomer conversion rate determination; charge-balanced point determination; fitting results for SAXS profiles; DSC profiles under multiple freezing/thawing cycles; variable-temperature SAXS/WAXS results; cross-sectional FE-SEM images of for hydrogel sample with different cooling rate (PDF)

## AUTHOR INFORMATION


### Corresponding Authors

*(H-J.C.) E-mail chung.hj13@ualberta.ca; phone +1-780-492-4790.

*(B.L.) E-mail blee@aps.anl.gov; phone +1-630-252-0395.

### ORCID

Xinda Li: 0000-0003-0670-8651

Guy M. Bernard: 0000-0003-1507-6705

Janet A. W. Elliott: 0000-0002-7883-3243

Vladimir K. Michaelis: 0000-0002-6708-7660

Byeongdu Lee: 0000-0003-2514-8805

Hyun-Joong Chung: 0000-0003-0569-6951


### Author Contributions

X.L. and H.-J.C. conceived ideas. X.L. and H.C. prepared and characterized hydrogels. J.A.W.E. provided critical insights into solution thermodynamics and ice formation. G.M.B. and V.K.M. performed, analyzed, and interpreted solid-state NMR experiments. B.L. performed, analyzed, and interpreted the SAXS and WAXS experiments. X.L. and H.-J.C. developed the model to explain the structure−property relations in polyampholyte hydrogels. X.L., J.A.W.E., G.M.B., V.K.M., B.L., and H.-J.C. wrote the manuscript.

### Notes

The authors declare no competing financial interest.

## ACKNOWLEDGMENTS

The authors gratefully acknowledge funding from a NSERC DG (RGPIN 435914). X.L. acknowledges an Alberta Innovates Technology Futures (AITF) Doctoral Scholarship. J.A.W.E. holds a Canada Research Chair in Thermodynamics. Material characterization was partly done in the shared facility of the NanoFAB in the Faculty of Engineering at the University of Alberta. The use of the Advanced Photon Source was supported by the U.S. DOE under Contract DE-AC02-06CH11357. The Natural Sciences and Engineering Research Council of Canada (RGPIN 05447) and the University of Alberta are acknowledged for generous NMR research support (V.K.M.).

## REFERENCES


(1) Peak, C. W.; Wilker, J. J.; Schmidt, G. A Review on Tough and Sticky Hydrogels. *Colloid Polym. Sci.* **2013**, *291*, 2031−2047.

(2) Zhao, X. Multi-Scale Multi-Mechanism Design of Tough Hydrogels: Building Dissipation into Stretchy Networks. *Soft Matter* **2014**, *10*, 672−687.

(3) Gong, J. P. Why Are Double Network Hydrogels So Tough? *Soft Matter* **2010**, *6*, 2583−2590.

(4) Alabarse, F.; Haines, J.; Cambon, O.; Levelut, C.; Bourgogne, D.; Haidoux, A.; Granier, D.; Coasne, B. Freezing of Water Confined at the Nanoscale. *Phys. Rev. Lett.* **2012**, *109*, 035701.

(5) Suzuki, Y.; Steinhart, M.; Graf, R.; Butt, H.-J.; Floudas, G. Dynamics of Ice/Water Confined in Nanoporous Alumina. *J. Phys. Chem. B* **2015**, *119*, 14814−14820.

(6) Liu, F.; Zargarzadeh, L.; Chung, H.-J.; Elliott, J. A. W. Thermodynamic Investigation of the Effect of Interface Curvature on the Solid−Liquid Equilibrium and Eutectic Point of Binary Mixtures. *J. Phys. Chem. B* **2017**, *121*, 9452−9462.

(7) Lv, J.; Song, Y.; Jiang, L.; Wang, J. Bio-Inspired Strategies for Anti-Icing. *ACS Nano* **2014**, *8*, 3152−3169.

(8) Wiener, C. G.; Tyagi, M.; Liu, Y.; Weiss, R. A.; Vogt, B. D. Supramolecular Hydrophobic Aggregates in Hydrogels Partially Inhibit Ice Formation. *J. Phys. Chem. B* **2016**, *120*, 5543−5552.

(9) Kudaibergenov, S. E. Recent advances in the study of synthetic polyampholytes in solutions. In *Polymer Latexes-Epoxide Resins-Polyampholytes*; Springer: 1999; pp 115−197.

(10) Dobrynin, A. V.; Colby, R. H.; Rubinstein, M. Polyampholytes. *J. Polym. Sci., Part B: Polym. Phys.* **2004**, *42*, 3513−3538.

(11) Goodman, C. M.; Choi, S.; Shandler, S.; DeGrado, W. F. Foldamers as Versatile Frameworks for the Design and Evolution of Function. *Nat. Chem. Biol.* **2007**, *3*, 252−262.

(12) Dill, K. A.; Ozkan, S. B.; Shell, M. S.; Weikl, T. R. The Protein Folding Problem. In *Annual Review of Biophysics*; Annual Reviews: Palo Alto, 2008; Vol. *37*, pp 289−316.

(13) Sun, T. L.; Kurokawa, T.; Kuroda, S.; Ihsan, A. B.; Akasaki, T.; Sato, K.; Haque, M. A.; Nakajima, T.; Gong, J. P. Physical Hydrogels Composed of Polyampholytes Demonstrate High Toughness and Viscoelasticity. *Nat. Mater.* **2013**, *12*, 932−937.

(14) Ihsan, A. B.; Sun, T. L.; Kurokawa, T.; Karobi, S. N.; Nakajima, T.; Nonoyama, T.; Roy, C. K.; Luo, F.; Gong, J. P. Self-Healing Behaviors of




DOI: 10.1021/acs.macromol.7b02498
*Macromolecules* 2018, 51, 2723−2731

Tough Polyampholyte Hydrogels. *Macromolecules* **2016**, *49*, 4245−4252.
(15) Sun, T. L.; Luo, F.; Kurokawa, T.; Karobi, S. N.; Nakajima, T.; Gong, J. P. Molecular Structure of Self-Healing Polyampholyte Hydrogels Analyzed from Tensile Behaviors. *Soft Matter* **2015**, *11*, 9355−9366.
(16) Chen, S.; Li, L.; Zhao, C.; Zheng, J. Surface Hydration: Principles and Applications toward Low-Fouling/Nonfouling Biomaterials. *Polymer* **2010**, *51*, 5283−5293.
(17) La, T.-G.; Li, X.; Kumar, A.; Fu, Y.; Yang, S.; Chung, H.-J. Highly Flexible, Multipixelated Thermosensitive Smart Windows Made of Tough Hydrogels. *ACS Appl. Mater. Interfaces* **2017**, *9*, 33100−33106.
(18) Roy, C. K.; Guo, H. L.; Sun, T. L.; Bin Ihsan, A.; Kurokawa, T.; Takahata, M.; Nonoyama, T.; Nakajima, T.; Gong, J. P. Self-Adjustable Adhesion of Polyampholyte Hydrogels. *Adv. Mater.* **2015**, *27*, 7344−7348.
(19) Li, X.; Liu, L.; Wang, X.; Ok, Y. S.; Elliott, J. A. W.; Chang, X. S.; Chung, H.-J. Flexible and Self-Healing Aqueous Supercapacitors for Low Temperature Applications: Polyampholyte Gel Electrolytes with Biochar Electrodes. *Sci. Rep.* **2017**, *7*, 1685.
(20) Zielinski, M. W.; McGann, L. E.; Nychka, J. A.; Elliott, J. A. W. Comparison of Non-Ideal Solution Theories for Multi-Solute Solutions in Cryobiology and Tabulation of Required Coefficients. *Cryobiology* **2014**, *69*, 305−317.
(21) Nisato, G.; Munch, J.; Candau, S. Swelling, Structure, and Elasticity of Polyampholyte Hydrogels. *Langmuir* **1999**, *15*, 4236−4244.
(22) Georgiev, G. S.; Kamenska, E. B.; Vassileva, E. D.; Kamenova, I. P.; Georgieva, V. T.; Iliev, S. B.; Ivanov, I. A. Self-Assembly, Antipolyelectrolyte Effect, and Nonbiofouling Properties of Polyzwitterions. *Biomacromolecules* **2006**, *7*, 1329−1334.
(23) Wang, F.; Yang, J.; Zhao, J. Understanding Anti-Polyelectrolyte Behavior of a Well-Defined Polyzwitterion at the Single-Chain Level. *Polym. Int.* **2015**, *64*, 999−1005.
(24) Schulz, D. N.; Peiffer, D. G.; Agarwal, P. K.; Larabee, J.; Kaladas, J. J.; Soni, L.; Handwerker, B.; Garner, R. T. Phase Behaviour and Solution Properties of Sulphobetaine Polymers. *Polymer* **1986**, *27*, 1734−1742.
(25) Huglin, M. B.; Radwan, M. A. Unperturbed Dimensions of a Zwitterionic Polymethacrylate. *Polym. Int.* **1991**, *26*, 97−104.
(26) Ye, T.; Song, Y.; Zheng, Q. Salt Response and Rheological Behavior of Acrylamide-Sulfobetaine Copolymer. *Colloid Polym. Sci.* **2016**, *294*, 389−397.
(27) Deek, J.; Chung, P. J.; Kayser, J.; Bausch, A. R.; Safinya, C. R. Neurofilament Sidearms Modulate Parallel and Crossed-Filament Orientations Inducing Nematic to Isotropic and Re-Entrant Birefringent Hydrogels. *Nat. Commun.* **2013**, *4*, 2224.
(28) Batchelder, L. S. *"Deuterium NMR in Solids" in eMagRes: the ultimate online resource for NMR and MRI*; Harris, R. K., Wasylishen, R. E., Eds. in chief; Wiley: DOI: 10.1002/9780470034590.emrstm0111 (posted online on Jan 14, 2009).
(29) Farrow, C. L.; Billinge, S. J. L. Relationship between the Atomic Pair Distribution Function and Small-Angle Scattering: Implications for Modeling of Nanoparticles. *Acta Crystallogr., Sect. A: Found. Crystallogr.* **2009**, *65*, 232−239.
(30) Gilbert, B. Finite Size Effects on the Real-Space Pair Distribution Function of Nanoparticles. *J. Appl. Crystallogr.* **2008**, *41*, 554−562.
(31) Kodama, K.; Iikubo, S.; Taguchi, T.; Shamoto, S. Finite Size Effects of Nanoparticles on the Atomic Pair Distribution Functions. *Acta Crystallogr., Sect. A: Found. Crystallogr.* **2006**, *62*, 444−453.
(32) Roe, R.-J. In *Methods of X-ray and Neutron Scattering in Polymer Science*; Roe, R.-J., Ed.; Oxford University Press: New York, 2000.
(33) Senesi, A. J.; Lee, B. Small-Angle Scattering of Particle Assemblies. *J. Appl. Crystallogr.* **2015**, *48*, 1172−1182.
(34) Bernard, G. M.; Goyal, A.; Miskolzie, M.; McKay, R.; Wu, Q.; Wasylishen, R. E.; Michaelis, V. K. Methylammonium Lead Chloride: A Sensitive Sample for an Accurate NMR Thermometer. *J. Magn. Reson.* **2017**, *283*, 14−21.
(35) Besselink, R.; ten Elshof, J. E. Mass-Fractal Growth in Niobia/Silsesquioxane Mixtures: A Small-Angle X-Ray Scattering Study. *J. Appl. Crystallogr.* **2014**, *47*, 1606−1613.
(36) Li, T.; Senesi, A. J.; Lee, B. Small Angle X-Ray Scattering for Nanoparticle Research. *Chem. Rev.* **2016**, *116*, 11128−11180.
(37) Hammouda, B. A New Guinier−Porod Model. *J. Appl. Crystallogr.* **2010**, *43*, 716−719.
(38) Everaers, R.; Johner, A.; Joanny, J.-F. Complexation and Precipitation in Polyampholyte Solutions. *EPL* **1997**, *37*, 275.
(39) Edwards, S.; King, P.; Pincus, P. Phase Changes in Polyampholytes. *Ferroelectrics* **1980**, *30*, 3−6.
(40) MacKnight, W.; Taggart, W.; Stein, R. A Model for the Structure of Ionomers. *J. Polym. Sci., Polym. Symp.* **1974**, *45*, 113−128.
(41) Gierke, T.; Munn, G.; Wilson, F. The Morphology in Nafion Perfluorinated Membrane Products, as Determined by Wide-and Small-Angle X-Ray Studies. *J. Polym. Sci., Polym. Phys. Ed.* **1981**, *19*, 1687−1704.
(42) Wang, N.; Ru, G.; Wang, L.; Feng, J. $^{1}$H MAS NMR Studies of the Phase Separation of Poly(N-isopropylacrylamide) Gel in Binary Solvents. *Langmuir* **2009**, *25*, 5898−5902.
(43) Jackson, J. A.; Rabideau, S. W. Deuteron Magnetic Resonance in Polycrystalline Heavy Ice ($D_2O$). *J. Chem. Phys.* **1964**, *41*, 4008−4008.
(44) Edmonds, D.; Mackay, A. The Pure Quadrupole Resonance of the Deuteron in Ice. *J. Magn. Reson.* **1975**, *20*, 515−519.
(45) Atkins, P.; De Paula, J. In *Elements of Physical Chemistry*, 5th ed.; Atkins, P., De Paula, J., Eds.; Oxford University Press: New York, 2009; pp 193−218.



DOI: 10.1021/acs.macromol.7b02498
*Macromolecules* 2018, 51, 2723−2731

# Supporting Information

# Low-Temperature Ionic Conductivity Enhanced by Disrupted Ice Formation in Polyampholyte Hydrogels

Xinda Li,[†] Hemant Charaya,[†] Guy M. Bernard,[‡] Janet A.W. Elliott,[†] Vladimir K. Michaelis,[‡] Byeongdu Lee,[§,*] Hyun-Joong Chung[†,*]

†Department of Chemical and Materials Engineering, University of Alberta, Edmonton, Alberta, T6G 1H9, Canada
‡Department of Chemistry, University of Alberta, Edmonton, Alberta, T6G 2G2, Canada
§Advanced Photon Source, Argonne National Laboratory, Argonne, Illinois 60439, U.S.A.

*E-mail: chung.hj13@ualberta.ca (H-J. Chung), phone: +1-780-492-4790
blee@aps.anl.gov (B. Lee), phone: +1-630-252-0395

# Contents in the Supporting Information:

Table S2. Fitting parameters for EIS measurements

## 10. $^{2}$H NMR Spectra of PA-10-2.1 and its Precursor, Acquired at −49 °C

Figure S11 $^{2}$H NMR spectra of non-spinning PA-10-2.1 and its precursor, acquired at −49 °C at 11.75 T.

## References (for Supporting Information)

## 1. Sample details

Table S1. The list of samples prepared.

| Sample | NaSS conc. | MPTC conc. | NaCl conc. | UV time |
|---|---|---|---|---|
| PA-6-2.1 | 1.07 M | 1.03 M | 6 wt% | 8 h |
| PA-8-2.1 | 1.07 M | 1.03 M | 8 wt% | 8 h |
| PA-10-2.1 | 1.07 M | 1.03 M | 10 wt% | 8 h |
| PA-10-1.05 | 0.536 M | 0.515 M | 10 wt% | 8 h |
| SOL-10-2.1 | 1.07 M | 1.03 M | 10 wt% | 0 h |

a. In all cases, 0.25 mol% photoinitiator (compared to the total concentration of NaSS and MPTC) was added in the precursor solution.

## 2. NaCl weight% in the as-prepared hydrogel

The weight% of NaCl in the as-prepared hydrogel is defined by Equation S1:

$$C_{\mathrm{NaCl}} = \frac{m_{\mathrm{NaCl}}}{m_{\mathrm{NaCl}}+m_{\mathrm{water}}} \times 100\% \qquad \text{(S1)}$$

where $m_{\mathrm{NaCl}}$ is the total mass of NaCl, and $m_{\mathrm{water}}$ is the mass of water added in the precursor solution. It is noted that NaSS and MPTC contain sodium and chloride ions, respectively which were accounted for in the calculation of the $m_{\mathrm{NaCl}}$ value.

## 3. The total monomer conversion rate determined by solution nuclear magnetic resonance (NMR) spectroscopy, and the leaching test.

The total monomer conversion rate was determined by $^{1}$H NMR spectroscopy. The NMR spectra were acquired on a Varian 600 MHz NMR spectrometer ($^{1}$H, 599.7 MHz) at room temperature. The water peaks were suppressed using pre-saturation pulses. First, as-prepared PA-10-2.1 was weighed and dissolved in a 4 M NaCl deuterium oxide solution overnight. The same mass of precursor solution for PA-10-2.1 was also diluted in the 4 M NaCl deuterium oxide solution. Weighed DSS (4,4-dimethyl-4-silapentane-1-sulfonic acid sodium salt) was added into both solutions as the internal standard substitute. The monomer conversion rate was determined by comparing the integrated peak area in the range of 7 to 5.5 ppm, which are proton signals from the alkene groups in the monomers (NaSS, and MPTC). The intensities of peaks were normalized based on the most intense signal from DSS, labeled 0 in both spectra. No obvious peak was observed in the PA-10-2.1 spectrum, indicating complete conversion after polymerization. A leaching test was also performed to measure the total monomer conversion rate by comparing the mass before and after dialysis. We assumed that the remaining unreacted monomers will leach out after one week dialysis in adequate deionized water. Based on the mass loss after considering the NaCl loss, the total monomer conversion rate was 98.1%.

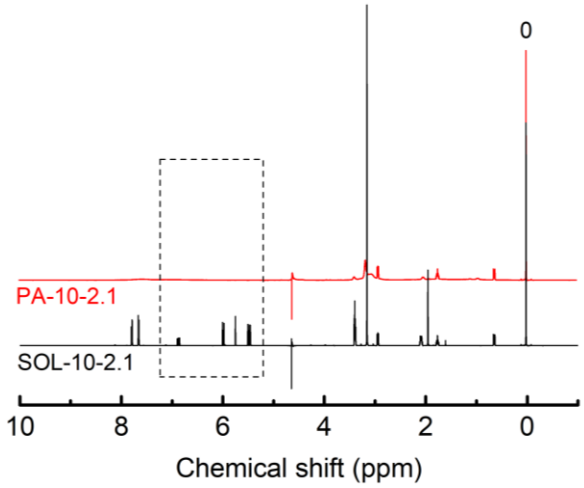


Figure S1. $^{1}$H solution NMR spectra for PA-10-2.1 and the precursor solution SOL-10-2.1 (including the monomers NaSS, and MPTC) at room temperature.

## 4. Charge-balanced point determination

All synthesized polyampholyte hydrogels in this paper were charge-balanced polyampholytes (*i.e.*, the amount of positively and negatively charged groups are the same in the hydrogel). It is important to experimentally determine the real feed monomer fraction to determine the exact charge-balance point. In a study on dilute aqueous solutions of polyampholytes, the coil size of the polyampholyte was shown to display a strong minimum at the charge-balance point.[1] Thus, the swelling ratio of the hydrogel will also show a minimum at the charge-balance point. We synthesized a series of polyampholyte hydrogels with various monomer factions. The total monomer concentration was fixed at 1.2 M, the NaCl concentration in the precursor solution was fixed at 10 wt% and the UV curing time was fixed at 8 h. The as-prepared hydrogels were dialyzed in deionized water for one week to achieve equilibrated swelling. The swelling ratio, $Q_{\mathrm{w}}$, is defined by Equation S2:

$$Q_{\mathrm{w}} = \frac{m_{\mathrm{equilibrium}}}{m_{\mathrm{as-prepared}}} \qquad \text{(S2)}$$

where $m_{\mathrm{equilibrium}}$ and $m_{\mathrm{as-prepared}}$ are the masses of the equilibrated and the as-prepared hydrogels. The results of the swelling experiments are shown in Figure S2. $Q_{\mathrm{w}}$ decreased before the MPTC fraction ($f_{\mathrm{MPTC}}$) reached 0.49 and sharply increased after this point, indicating that coulombic attraction prevails over the repulsion and the polymer chains collapse near the charge-balance point ($f_{\mathrm{MPTC}}$= 0.49).

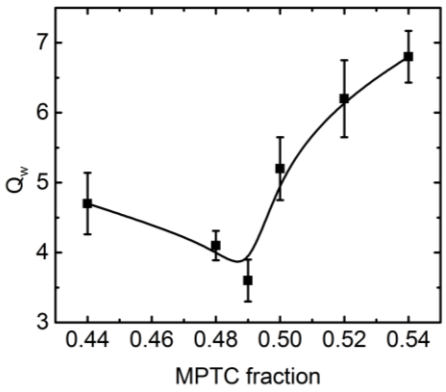


Figure S2. Swelling ratio as a function of MPTC fraction.

## 5. DSC profiles under multiple freeze–thaw cycles

The polyampholyte hydrogels were measured by differential scanning calorimetry (DSC, Q1000, TA Instruments, US) at a cooling rate of 0.5 °C/min.

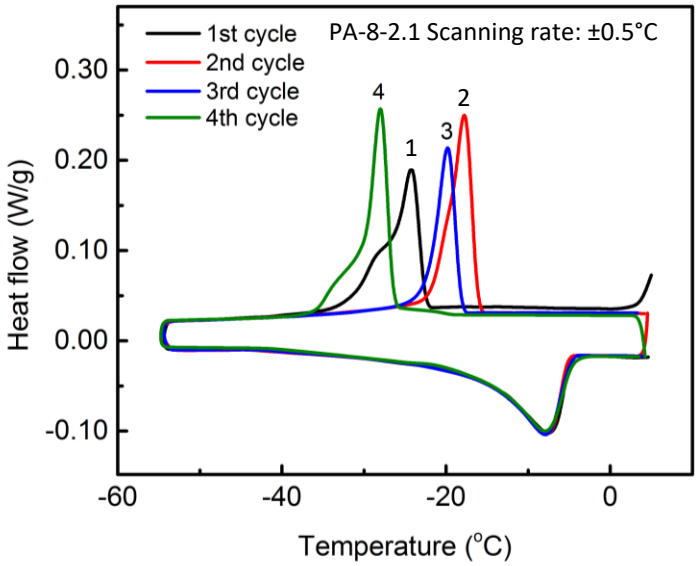


Figure S3. Raw DSC profiles (thawing) for PA-10-2.1 under multiple freeze–thaw cycles.

## 6. Development of SAXS Theory for Clusters

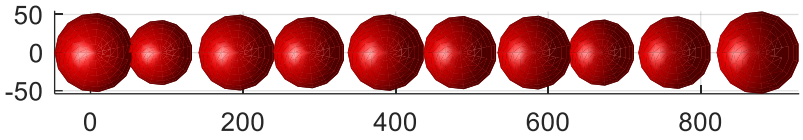


Figure S4. A model 1D array of spheres. Length *L* of the model is the center-to-center distance between the first and last spheres. The model is composed of 10 spheres with mean radius 5 nm and 12% size variation. The gaps between the particles are set to 0.5 nm.

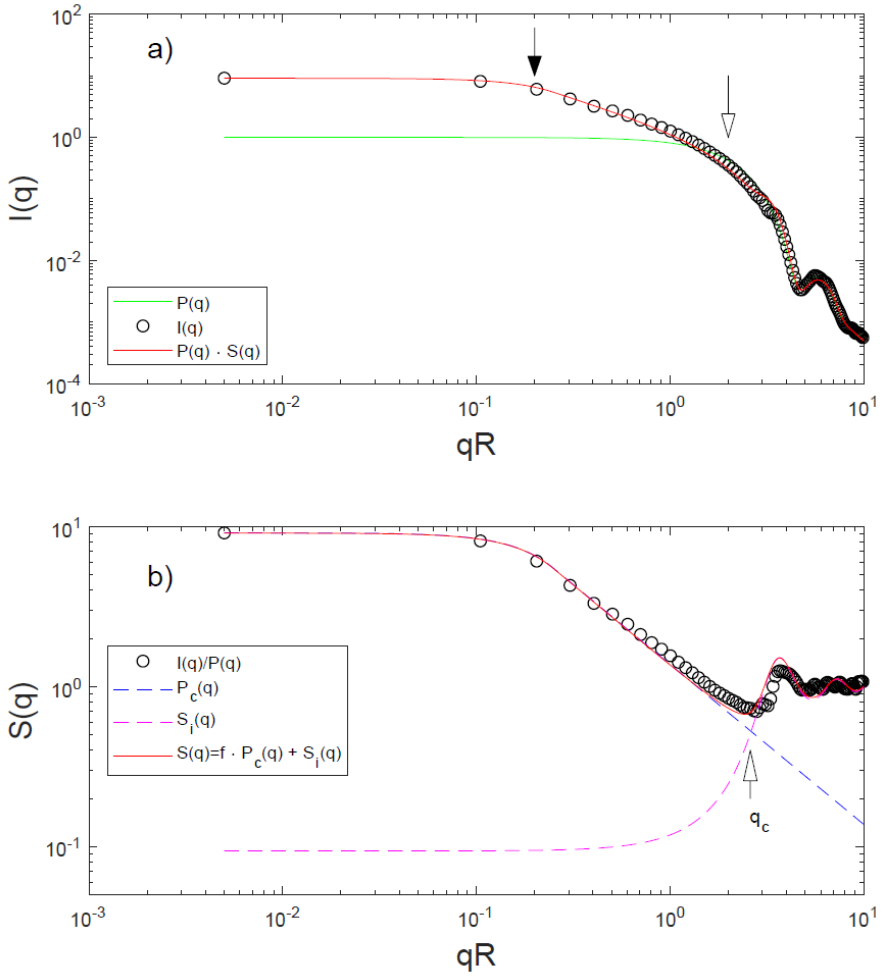


Figure S5. a) Simulated intensity $I(q)$ and form factor $P(q)$ from the model in Figure S4. b) $I(q)/P(q)$ is approximated with the structure factor model shown in the equation above.

### 6.3 Application to Data Analysis

We analyzed SAXS data with this theory and plotted all components for each data fit in Figure S6. Internal structure factor is found for a) and b) with volume fractions of about 2%. Interestingly the hydrodynamic radius for the PY structure factor decreases with increasing salt concentration, reflecting the reduction of repulsive interaction due to charge screening. Clustering is observed with higher concentrations of NaCl and lower monomer concentrations, suggesting hydrophobic interactions may play a role.

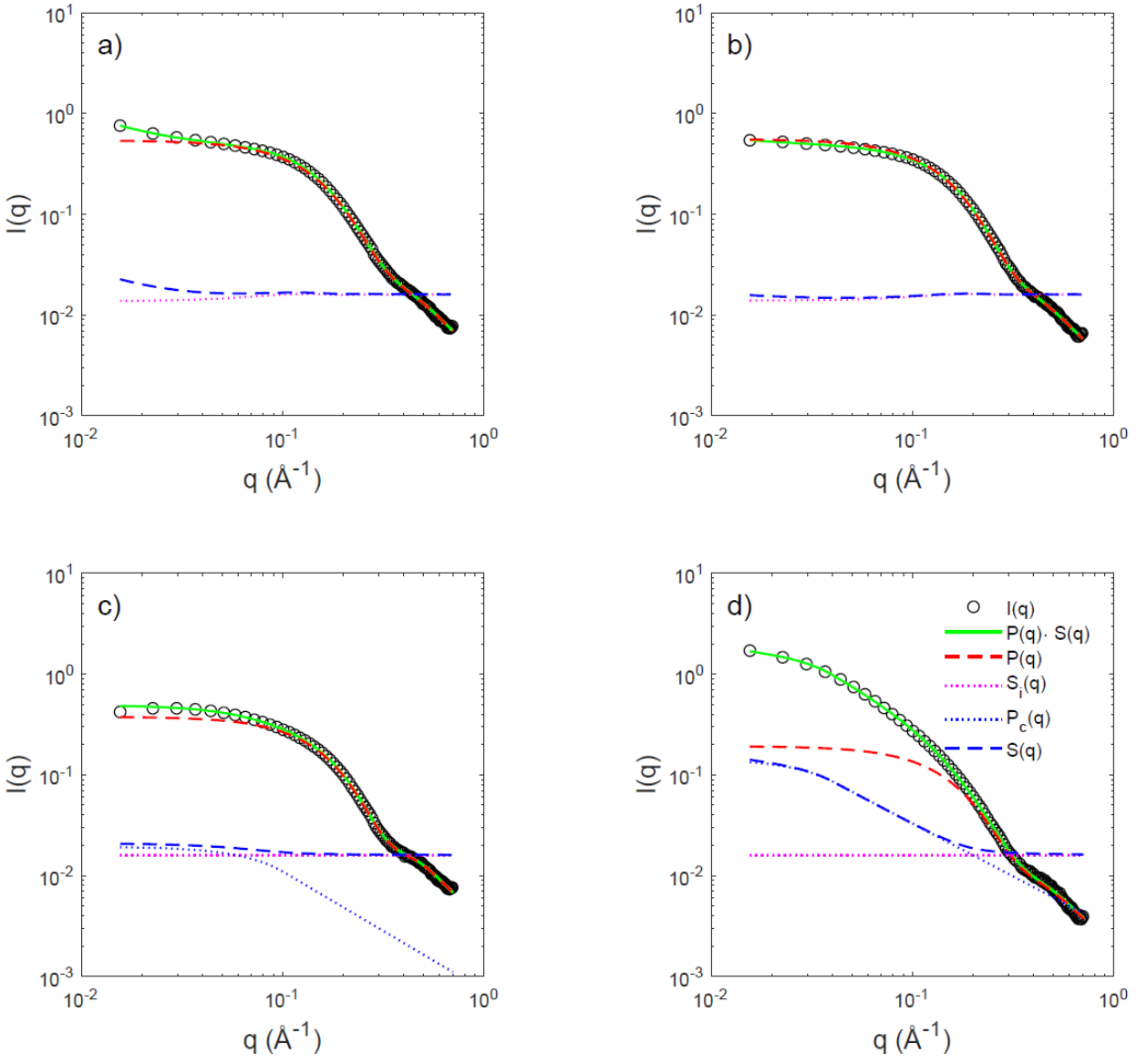


Figure S6. Measured intensities and calculated $P(q)$, $S(q)$, $P_c(q)$, and $S_i(q)$. PA-6-2.1, PA-8-2.1, PA-10-2.1 and PA-10-1.05 for a) through d), respectively.

## 7. Variable-temperature SAXS and WAXS results

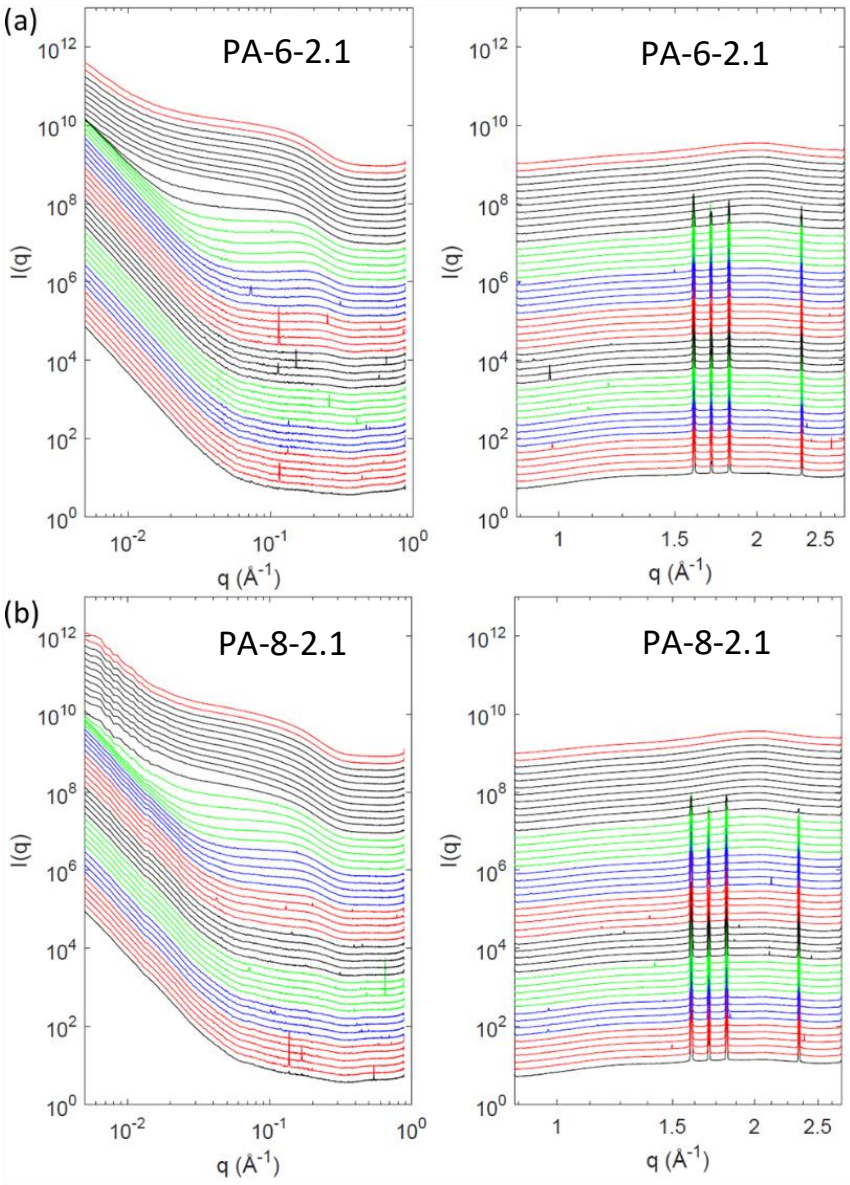

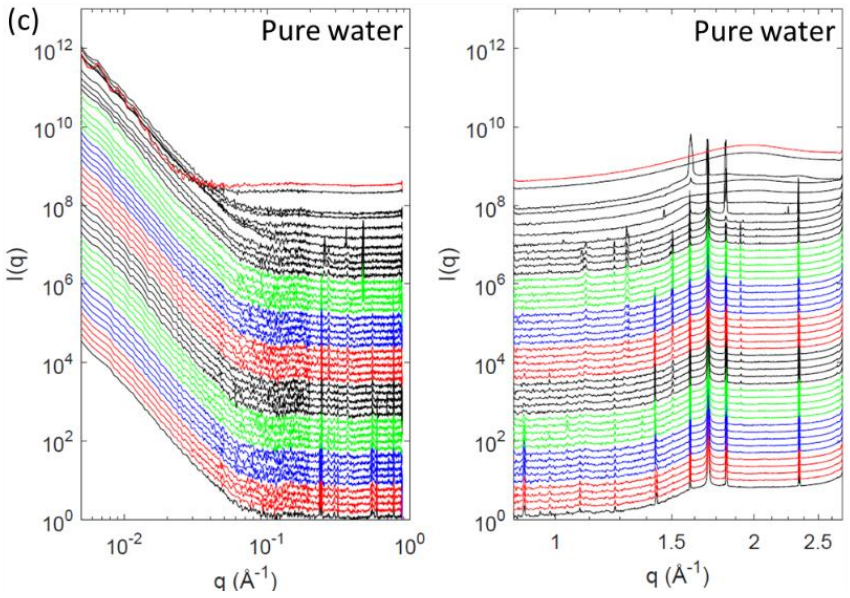


Figure S7 SAXS (left column) and WAXS (right column) spectra of (a) PA-6-2.1, (b) PA-8-2.1, and (c) pure water. Here, the background of SAXS spectra were subtracted by an empty glass tube (The SAXS spectra in the main text were subtracted by glass tubes filled with salt water with the respective NaCl concentration.)

## 8. Cross-sectional FE-SEM images of hydrogel samples with different cooling rates.

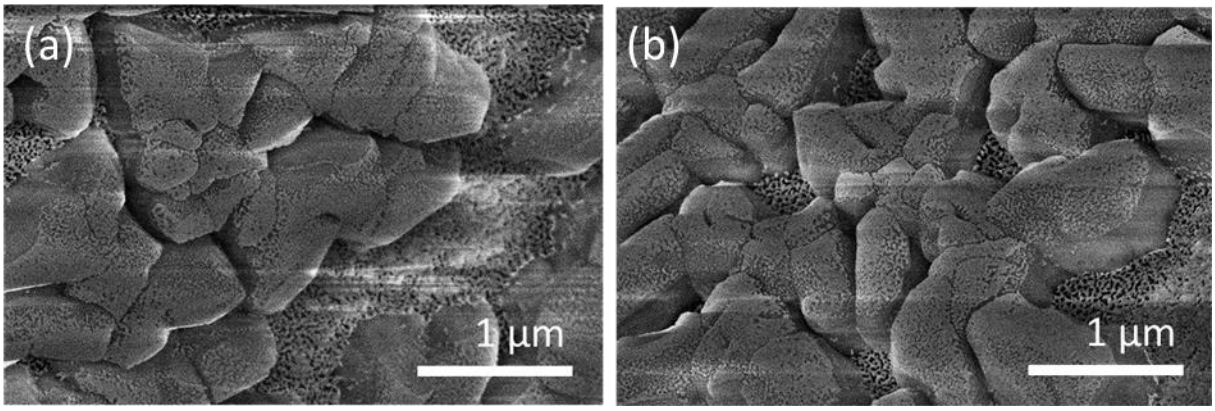


Figure S8. Cross-sectional FE-SEM images of PA-10-2.1 pre-frozen at –30 °C, at a rate of (a) 0.5 °C/min, and (b) 5 °C/min using a temperature-control chamber, and held at –30 °C for 30 min, followed by quenching in liquid nitrogen, and freeze-drying.

## 9. Analysis for Electrochemical Impedance Spectroscopy (EIS) Measurement

Conductivity values of the three electrolyte systems at temperatures ranging from +20 °C to −30 °C were measured in the cell placed in a Peltier stage (TS102G, Instec Inc.), as described in "Experimental Section" in the main text. The EIS results for the 10 wt% NaCl solution, SOL-10-2.1 and PA-10-2.1 are shown in Figure S9.

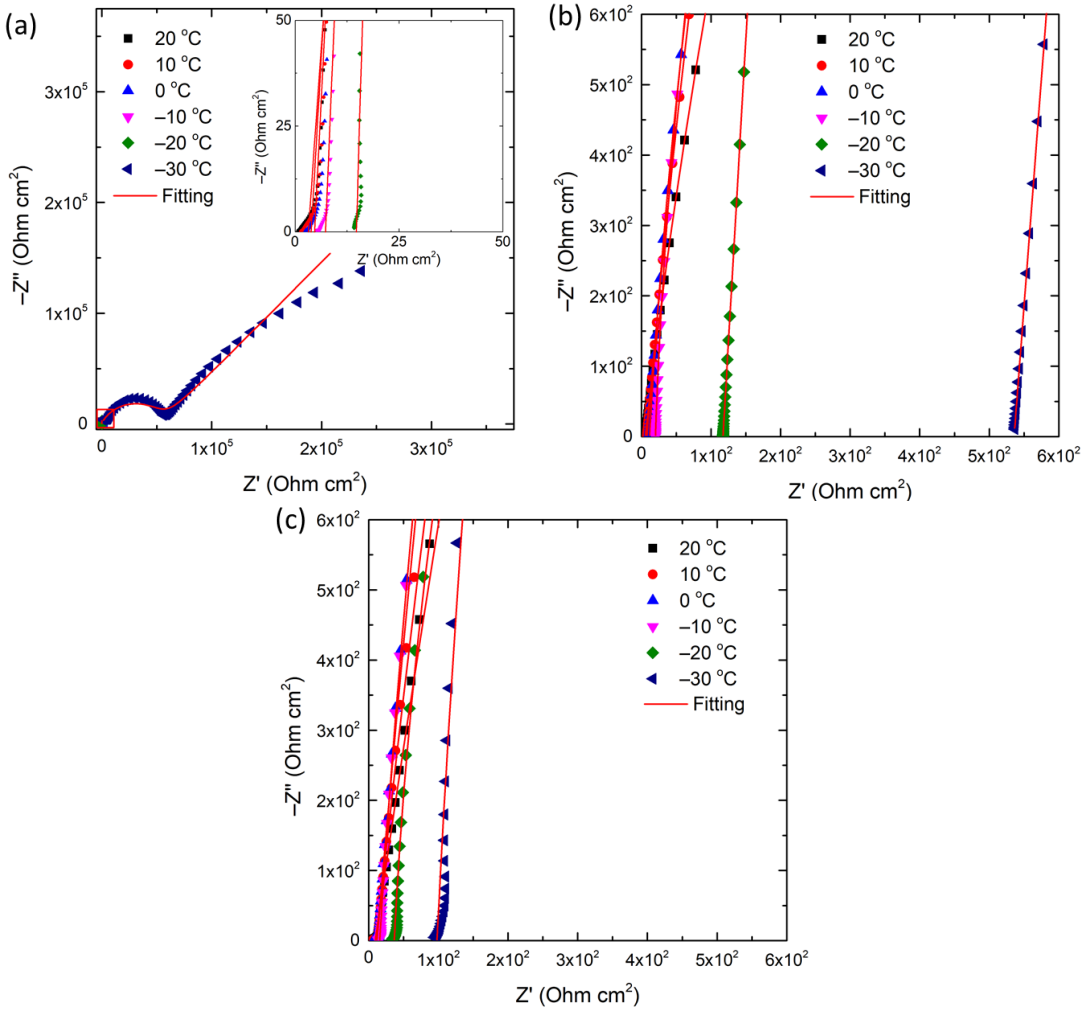


Figure S9. EIS results for (a) 10 wt% NaCl solution, (b) SOL-10-2.1 and (c) PA-10-2.1 at various temperatures. The inset in (a) is the magnified part of the region identified by the red box in the left-bottom corner of (a). Red solid lines were the fitting using the Randles circuit model.

We followed the general approach of determining the various parameters of an electrochemical system by fitting the impedance data to an equivalent electrical circuit. We used the Randles circuit model for data fitting as it physically interprets our electrochemical cell in the

best possible manner.[2-4] Figure S10 represents a circuit model of a Randles cell which typically consists of four components: solution resistance ($R_s$), a constant phase element (*CPE*), charge transfer or polarization resistance ($R_{CT}$) and a Warburg diffusion element ($Z_W$). In physical terms, $R_s$ corresponds to resistance against the migration of ions inside the electrolyte (solution or hydrogel); CPE corresponds to an imperfect double layer capacitor that forms at the interface between the electrode and surrounding electrolyte; $R_{CT}$ is the charge transfer resistance for kinetically controlled electrochemical reaction taking place at the interface between the electrode and electrolyte; $Z_W$ accounts for the diffusional impedance of the electrochemical system. The focus of our study is to extract the values of $R_s$ at different temperatures, as shown in Table S2. In order to calculate the conductivity of the electrolyte, we used the following relation:

$$\kappa = \frac{c}{R_s} \qquad \text{(S15)}$$

, where $c$ is the cell constant, which is a characteristic parameter of the experiment setups, and $R_s$ is the solution resistance.

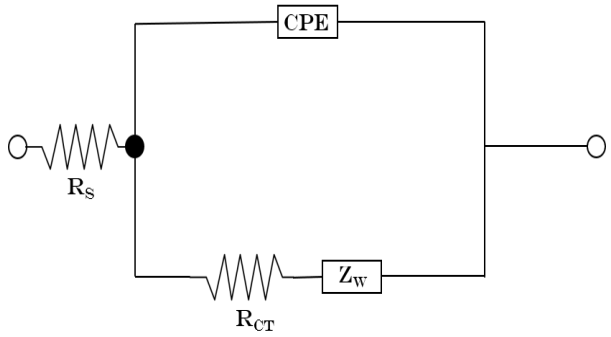


Figure S10: Equivalent Randles circuit for modelling of impedance data of the electrolyte system.

Table S2. Fitting parameters for EIS measurements

| **Temperature** | **10 wt% NaCl solution** | | **SOL-10-2.1** | | **PA-10-2.1** | |
|---|---|---|---|---|---|---|
| **(°C)** | $R_s$(Ω cm$^2$) | % error | $R_s$(Ω cm$^2$) | % error | $R_s$(Ω cm$^2$) | % error |
| **20** | 2.05 | 0.55 | 5.18 | 0.48 | 8.87 | 0.57 |
| **10** | 2.70 | 0.56 | 7.57 | 0.39 | 9.77 | 0.76 |
| **0** | 3.56 | 0.49 | 11.24 | 0.53 | 11.31 | 0.70 |
| **−10** | 6.17 | 0.33 | 19.79 | 0.51 | 15.68 | 1.08 |
| **−20** | 13.64 | 0.37 | 116.89 | 0.58 | 36.13 | 0.46 |
| **−30** | 4656.79 | 9.47 | 536.11 | 0.83 | 97.39 | 0.78 |

## 10. $^{2}$H NMR Spectra of PA-10-2.1 and its Precursor, Acquired at −49 °C

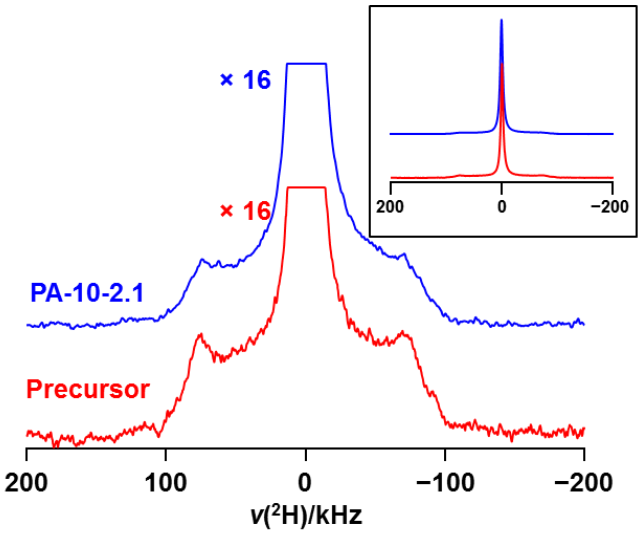


Figure S11 $^{2}$H NMR spectra of non-spinning PA-10-2.1 and its precursor, acquired at −49 °C at 11.75 T. The vertical intensity has been multiplied by 16 to emphasize the broad underlying powder pattern; the inset illustrates the complete spectra.

## References (for Supporting Information)

1. Dobrynin A.V.; Colby R.H.; Rubinstein M. "Polyampholytes". *Journal of Polymer Science Part B: Polymer Physics* **2004**, *42(19)*, 3513–3538.

2. Yu H.; Wu J.; Fan L.; Xu K.; Zhong X.; Lin Y.; Lin J. "Improvement of the performance for quasi-solid-state supercapacitor by using PVA–KOH–KI polymer gel electrolyte". *Electrochimica Acta*. **2011**, *56(20)*, 6881–6886.

3. Nohara S.; Wada H.; Furukawa N.; Inoue H.; Morita M.; Iwakura C. "Electrochemical characterization of new electric double layer capacitor with polymer hydrogel electrolyte". *Electrochimica Acta*. **2003**, *48(6)*, 749–753.

4. Sun K.C.; Arbab A.A.; Sahito I.A.; Qadir M.B.; Choi B.J.; Kwon S.C.; Yeo S.Y.; Yi S.C.; Jeong S.H. "A PVdF-based electrolyte membrane for a carbon counter electrode in dye-sensitized solar cells". *RSC Advances* **2017**, *7(34)*, 20908–20918.